Metals and Materials International
https://doi.org/10.1007/s12540-025-02211-3

Analyzing the Effect of Fe on the Microstructure and Mechanical Properties of a Fibrous AA6110 Alloy

Fazlollah Sadeghi[1] · Nilam Barekar[2] · Tungky Subroto[2] · Pavel Shurkin[1] · Geoff Scamans[1,3] · Carla Barbatti[2,4]

Received: 3 October 2025 / Accepted: 15 December 2025

Abstract

In this study, the effect of three different levels of iron impurity on the grain structure and texture of a fibrous AA6110 alloy after hot extrusion was investigated. Microstructural examination was carried out to measure the microtexture and the results were correlated with tensile and bending mechanical properties. Results demonstrated that the fragmented intermetallic particles after extrusion stimulate the nucleation of new grains, therefore refining the grain structure. The thickness of peripheral coarse grains was found to decrease by increasing Fe content due to increasing nano-sized dispersoid precipitation density. Increment Fe-rich intermetallics on the one hand leads to entrapment of Si solute reducing free Si needed for precipitation hardening shown via thermodynamic calculations. The bending formability was found to correlate with the grain structure of the PCG thickness. The results are compared with Part 1 of this research on the study of Fe content in recrystallized alloys. This work helps to a better understanding of recyclability in Al extrusion alloys.

Keywords Al alloys · Texture · Dynamic recrystallization · Fibre texture · Fe-based intermetallics

1 Introduction

The production of lightweight components through a combination of direct chill (DC) casting of aluminum alloys (AA) followed by hot extrusion has proven to be an effective process for both structural and transportation-related applications [1–3]. The Al–Mg–Si series have been frequently produced via hot extrusion methods due to the combination of good extrudability, surface finish, good corrosion resistance [4], and relatively high mechanical properties. These properties make them ideal for structural components and exterior panels in automotive applications, where their high ductility plays a crucial role in absorbing energy during deformation events, such as vehicle collisions [2, 5]. The performance of these alloys is closely linked to microstructural characteristics like grain structure and crystallographic texture, which in turn are influenced by the alloy composition, production route, and processing parameters [6–11]. Goik et al. [12] demonstrated that increasing the extrusion speed during the production of hollow box profiles reduced the intensity of *β-fibre* texture components in both recrystallized and fibrous microstructures, while increasing the thickness of the peripheral coarse grain (PCG) zone and enhancing Cube recrystallization texture.

From the chemical composition point of view, the existence of Mg and Si as the main element additions leads to the formation of Mg_2Si precipitates at temperatures below the solvus after a supersaturated solid solution. Precipitation hardening mechanism is the main factor for tailoring the microstructure to obtain desired mechanical properties [13–15]. Other alloying elements also influence the final product properties. For instance, Mn, Cr, and Zr are mainly retained in solid solution after casting and precipitate during homogenization in the form of nano-sized precipitates, so-called dispersoids, preferably at the high-angle grain boundaries (HAGB) [16–20]. Dispersoids hinder grain boundary migration during deformation at elevated temperatures

✉ Fazlollah Sadeghi
fazlollah.sadeghihosnijeh@brunel.ac.uk

1 Brunel Centre for Advanced Solidification Technology (BCAST), Brunel University London, Uxbridge, Middlesex UB8 3PH, UK

2 Constellium University Technology Centre, Brunel University London, Uxbridge, Middlesex UB8 3PH, UK

3 Innoval Technology, Unit 9 Selden Way, S60 5AA Rotherham, UK

4 Constellium Technology Center, Parc Economiqye Centr'Alp, CS 10027, , 38341 Voreppe Cedex, France

preventing grain growth. Using Mn to form dispersoids has been shown to be successful in increasing strength at elevated temperatures in wrought Al-Si series [21–24], Al–Mg [25, 26], and Al–Mg–Si series [19, 27–29]. Iron (Fe), on the other hand, tends to form various intermetallic compounds (IMCs) with Al, Si, and Mn during solidification [30–32], which cannot be dissolved in further heat treatment processes. These particles are detrimental to the mechanical properties of various product components [6, 33]. Analysis of the Al alloy die cast products has shown [34–36] a detrimental trend in ductility and tensile strength of the Al–Mg–Si alloys. However, die cast components have a near-cast structure where morphological aspect of needle-shape IMC particles play an important role.

In addition to the effect of dispersoid forming elements (DFE) [28, 37, 38], highly soluble alloying elements in a face-centred cubic (FCC) matrix as a solid solution can affect the stacking fault energy (SFE), therefore triggering different deformation mechanisms to accommodate deformation depending on the SFE level. In low SFE materials such as stainless steels [39–42], planar slip is favoured and this facilitates twinning. By contrast, in high SFE materials such as aluminium alloys, the material hardly forms twinning and dislocation cross-slip dominates instead [12, 43]. Whereas the effect of iron on AA6xxx alloys has been discussed widely in terms of solidification, phase composition and influence on precipitation hardening [44–46], its influence on grain structure and texture after industrial scale extrusion remains ambiguous. Goik et al. have studied the fibrous 6082 and 6005 alloys in terms of Fe addition and claimed that iron helps retain fibrous microstructure due to an increase in the dispersoids' fraction; although, it's not clear whether this effect is a result of Fe addition or DFEs (Mn and Cr) [12]. Despite the high Mn content, stronger recrystallization and grain growth was observed due to particle-stimulated nucleation (PSN) [44, 47]. The Fe-based IMCs, particularly α-Al(FeMnCr)Si, can influence the texture during thermomechanical processes. By the accumulation of deformation in the surroundings of IMCs, a set of newly equiaxed grains possessing a texture that is deflected from the standard one can occur [48]. Although PSN is a well-known phenomenon and reported in cold-rolled AA8xxx [49, 50] up to 0.7 wt%, hot-extruded AA7xxx [51],

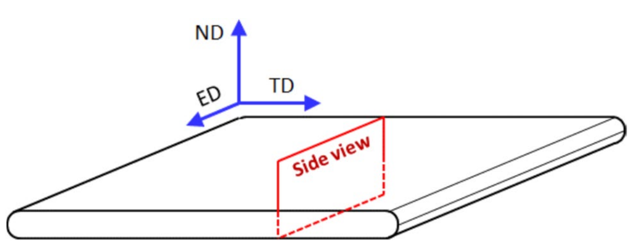

Fig. 1 Schematic representation of extruded profile and sampling region from the side view

rolled Al–Mg alloy [52], it has not been reported in extruded Al–Mg–Si profiles. Our observations of PSN helps to clarify the effects of Fe addition to microstructural and mechanical properties in extrusion industry of the Al–Mg–Si alloys.

Although AA6xxx series alloys are widely used and essential for promoting sustainability and reducing carbon footprints through recyclable materials, the impact of Fe as a single impurity in an industrial fibrous alloy after hot extrusion has not been thoroughly explored especially considering the effect of particle stimulated nucleation and subsequent consequences on grain structure, texture, and dynamic recrystallization. To address this, an AA6110 alloy exhibiting a fibrous grain structure was investigated. Another part of this research work focusing on the effect of Fe in recrystallized AA6008 alloy has been published elsewhere. While alloys with fibrous structure exhibit high strength, recrystallized alloys having dominant cube texture show high ductility mainly used for crush performance. We have reported a complex behaviour when additional Fe results in formation of more IMC compounds within the Al matrix [Under Review]. A comprehensive microstructural and mechanical investigation were carried out on the influence of Fe content in hot extruded profiles.

2 Materials and Methods

The AA6110 with a fibrous microstructure was used for this study. It should be noted that the effect of Fe on recrystallized AA6008 is currently under review elsewhere. Three variations of the AA6110, having Fe content of 0.2wt%, 0.3wt%, and 0.5 wt% were direct chill (DC) cast into billets, homogenized [53], and extruded into flat strips as shown schematically in Fig. 1 in an industrial scale. The aim is to keep all influential process parameters and chemical composition constant except for the level of Fe. The 0.2Fe, 0.3Fe, and 0.5Fe names will be used for identification of the alloys henceforth.

Firstly, the extruded samples were artificially aged to T6 temper according to suggested cycles from Ref. [54] to achieve desired tensile strength. Then, samples were cut from the profile as shown schematically in Fig. 1 for characterisation. Tensile and bending tests were then performed on an Instron universal tensile machine following the standard procedures according to BS EN ISO 6892-1 [55] and VDA 238-100 [56]. The bending test is performed in a 3-point bend test, where a sample supported on both sides is loaded at its centre point and bent to a specific angle or until the test sample fails. The average bending angle is then measured to report as a criterion of formability.

For microstructural examinations, the longitudinal cross-section of samples was prepared using standard metallographic procedures, polished to colloidal silica, followed by electropolishing using 30% nitric acid in methanol at −30 °C at 15 V. For EBSD analysis, a scanning electron microscope (SEM) (TESCAN Magna) was used at an accelerating voltage of 15 keV and 30nA probe current to obtain electron back-scattered diffraction (EBSD) data as well as energy dispersive spectroscopy (EDS). Extraction of the EBSD results was carried out using Oxford Aztec v6.0 and data acquisition using Aztec Crystal v3.1. TEM was used for observation of Nano-sized dispersoid particles. Samples were prepared by grinding thin specimens down to 100 µm followed by punching a 3 mm disk and jet polishing via Struers TenuPol-5 with the 25% nitric acid in methanol at -25 °C. The Talos F200i field emission transmission electron microscopy (FETEM) facility was used equipped with EDS Bruker. Thermodynamic calculations were performed using Pandat software and PanAl2021 database.

3 Results and Discussion

3.1 Effect of Fe on Microstructure

The overview picture of the profiles' microstructure after extrusion is shown in Fig. 2, where it shows fibrous grain structures. The effect of Fe on the peripheral coarse grains (PCG) depth can be seen straightaway. Quantification of the PCG thickness in extruded alloys has been a common practice in industry [12, 57]. In contrast to the results of Hovden et al. [47], our present investigation of the alloy with a fibrous grain structure concluded that the addition of iron does not affect the fibrous microstructure. Moreover, the higher magnification images at certain points presented in Fig. 2d–f were utilized for analysis of PCG at different extrudate lengths. Statistical measurements show that the PCG depth in this alloy decreases with iron content from 137 ± 30 µm for 0.2Fe, to 106 ± 17 µm for 0.3Fe, and to 64 ± 10 µm for 0.5Fe, respectively. The mechanism of PCG thickness reduction by increasing Fe content will be further discussed in the following section.

The formation of peripheral coarse grains at the extruded profile's surface [57–59] is influenced by chemical composition as well as process parameters. Goik et al. found that increasing Fe + Mn + Cr content resulted in a reduction in PCG thickness [12], but the effect of single iron addition was not studied. Apart from the effect of process parameters, it has been reported that the existence of Mn as a dispersoid-forming element in an AA6082 alloy [28] results in precipitation of dispersoids increasing Zener-drag pressure and preventing recrystallization. Based on optical microscopy observations, one can conclude that the recrystallized alloys do not change their nature due to an increase in iron as the latter does not form pinning particles and Mn content remains rather low. Similarly, increased iron content does

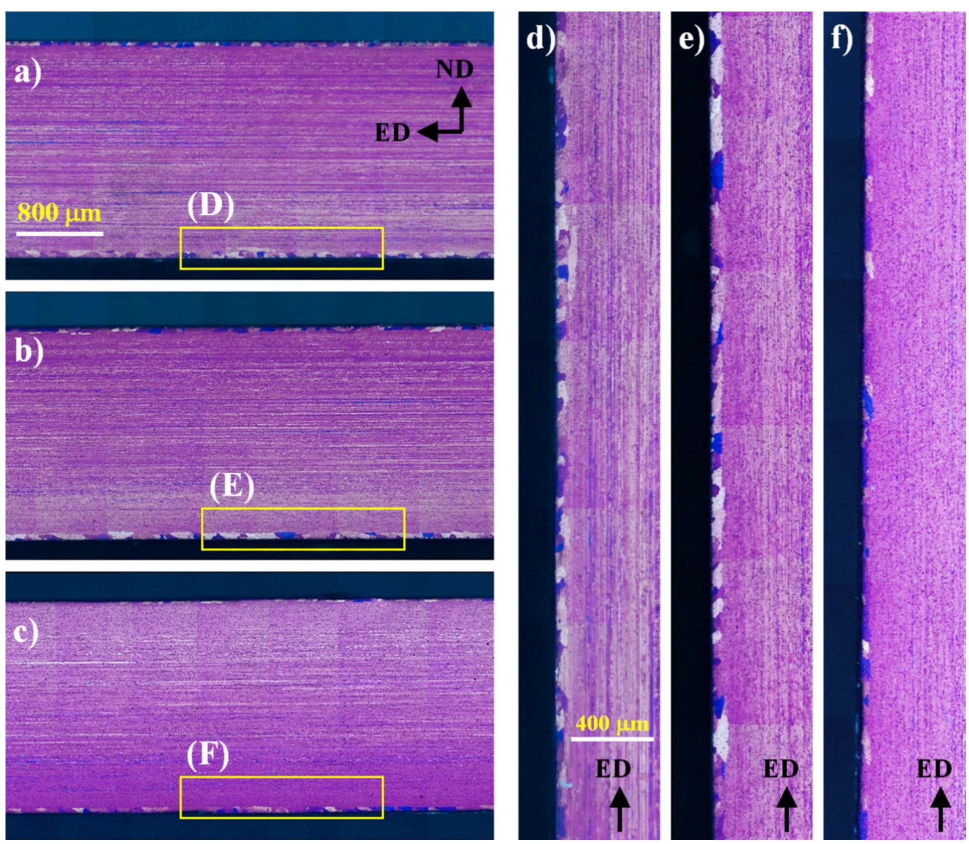

Fig. 2 Optical microscopy images of **a** 0.2Fe, **b** 0.3Fe and **c** 0.5Fe alloys extrudate profiles all at same magnification along with zoomed images for PCG clarification at profile peripheries

not cause any significant PSN effect in fibrous alloys, which means that the dispersoid's pinning pressure still helps to limit grain boundary migration. For both cases, EBSD analysis will help to quantify more precisely the differences in grain size and their orientations, which are determining factors for mechanical properties.

The effect of iron on the area fraction of IMC particles was investigated by quantitative metallography on the BSE images taken at the centre of profile thickness presented in Fig. 3. Visual inspection clearly shows an increasing trend in the Fe-based IMC particles along the extrusion direction due to an extremely low solubility of Fe in Al [60]. Due to a high contrast difference between Al matrix (dark grey) and Fe-IMC particles (white particles) in SEM-BSE images, quantifying the distribution of phases is feasible via image analysis. Thus, 3 images were taken for each condition and image analysis was performed using the ImageJ software to analyze the particles and corresponding area fraction histogram for each sample.

In this alloy, existing iron will contribute in two ways. In addition to the formation of Fe-IMC particles during solidification, secondary Nano-sized dispersoid particles also form during high-temperature homogenization treatment due to the presence of Mn in fibrous AA6110. The size, distribution, and number density of dispersoid particles depend on the process parameters and chemical composition. By studying the effect of Mn and Zr addition to AA6082, Elasheri [20] et al. have reported that dispersoid precipitation can effectively reduce PCG thickness layer and high retention of strong deformation texture. Osterreicher et al. [61] have studied the effect of process parameters (*i.e.* cooling and heating rate as well as homogenization temperature) on the microstructural evolution of an AA6xxx series alloy. Since the dispersoid particles prevent nucleation by pinning grain boundaries as explained by the Zener drag pressure effect [48, 57], it can be inferred that at the same processing condition, an increase in density of dispersoid particles results in reduction of PCG thickness. The difference between the size, distribution, and composition of the Fe-based IMCs and dispersoid particles were measured from high-angle annular dark field (HAADF) scanning transmission electron microscopy bright field (STEM-BF) representative images of alloys in different Fe contents presented in Fig. 4.

A quantification of both Fe-containing IMCs and dispersoid precipitates comparison was carried out and plotted in Fig. 5 obtained from an average of 7 images at each condition. The IMCs were analyzed via BSE-SEM images (one sample image is shown in Fig. 3) and dispersoids were analyzed from HAADF-STEM images (one sample image is presented in Fig. 4). According to Fig. 5a, the area fraction of IMC particles increases by increasing Fe content; but the circularity remains the same. Minoda et al. have reported a similar trend in increasing size and number density of Fe-based IMC particles by increasing Fe content [62]. Due to the complexity of Fe-based IMC formation during solidification, and its inability to dissolve during homogenization treatment, and processing [63], the circularity of the IMCs does not change by increasing Fe content. The quantitative particle analysis of dispersoids depicted in Fig. 5b shows a similar trend in number density increment by increasing Fe content in this alloy.

To estimate the evolution of phases and composition by changing Fe content of the alloy, thermodynamic calculations were performed and presented in Fig. 6. The fibrous alloy, which contains high Mn content, shows a simple phase composition-temperature relationship and only α-$Al_9Fe_2Si_2$ can forms (Fig. 6b). As shown in the phase fraction calculations in Fig. 6b with an increase in Fe content, the total fraction of Fe-based IMCs increases sharply, while the Si solute in the (Al) matrix decreases. This is noteworthy to mention that the Si in Al matrix is the available free Si dissolved in Al after some Si content is being consumed by Fe-based IMCs. This affects the precipitation hardening response which will be discussed later. Conclusively, it can be derived that the addition of Fe has contributed to the addition of Fe-rich IMCs as well as dispersoid precipitations when comparing thermodynamic calculations (Fig. 6) with experimental area fraction measurements (Fig. 5).

To evaluate the crystalline orientations corresponding to the grain structure in each investigated condition, EBSD

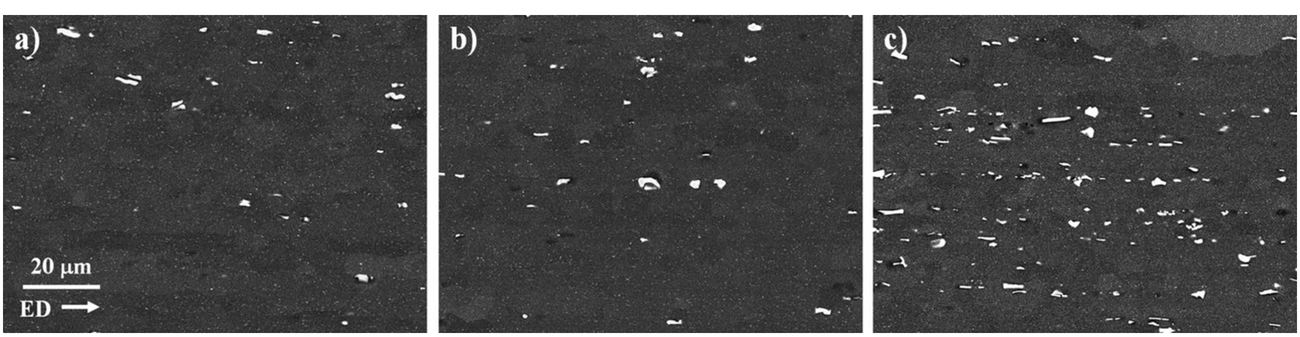

Fig. 3 SEM/BSE images taken at the same magnification at **a** 0.2Fe, **b** 0.3Fe, and **c** 0.5Fe content accompanied by histogram of corresponding area fraction

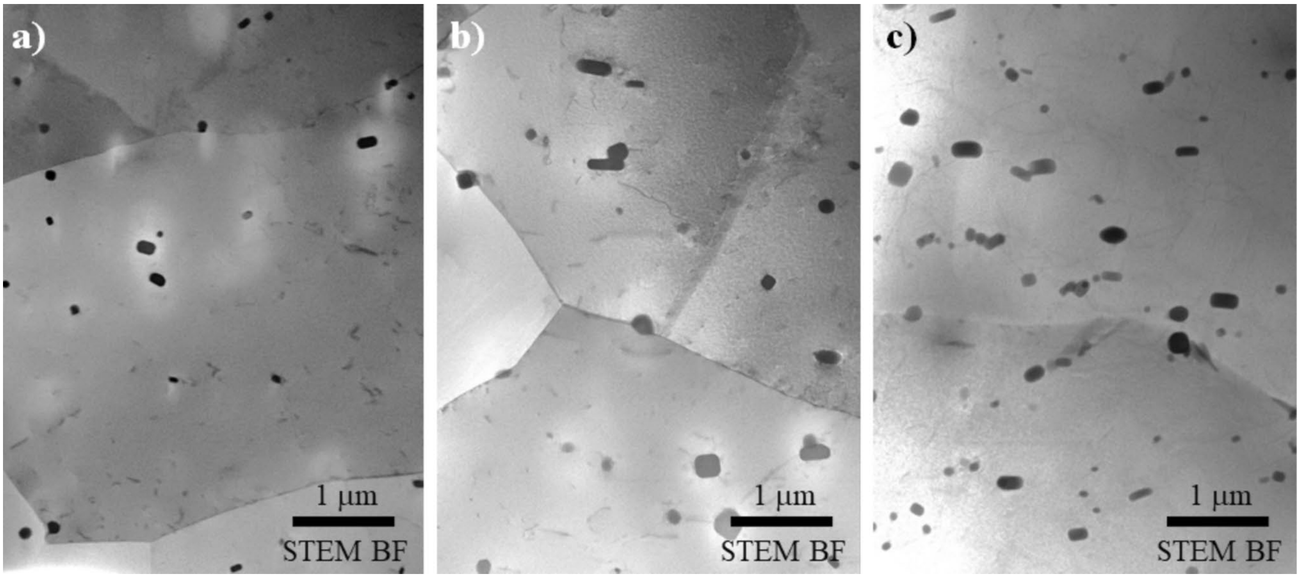

Fig. 4 STEM-BF images obtained from dispersoids precipitation taken from **a** 0.2Fe, **b** 0.3Fe, and **c** 0.5Fe alloys

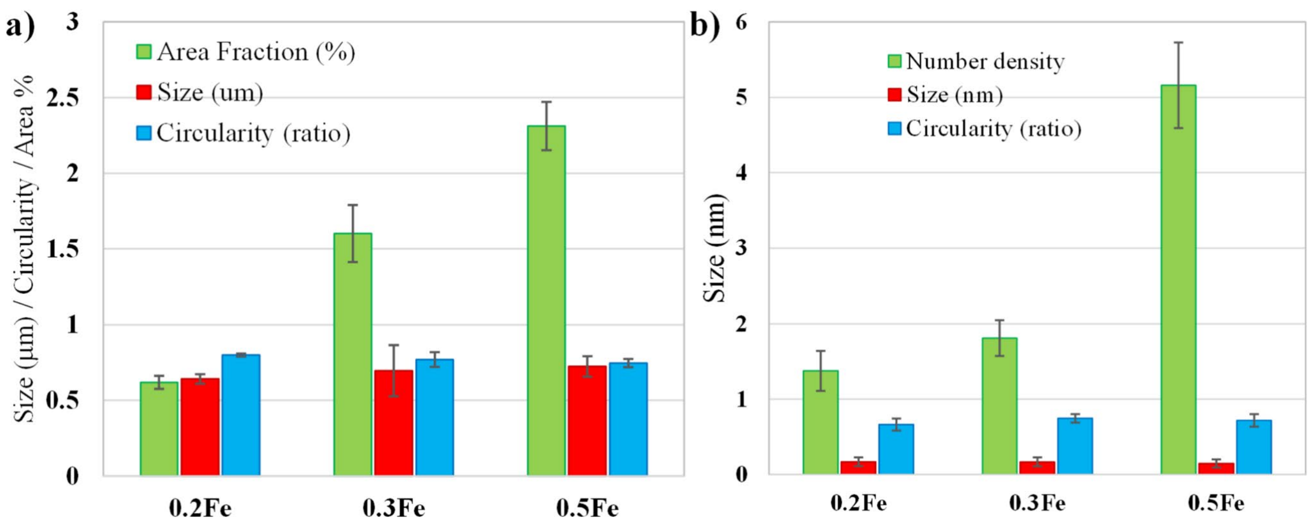

Fig. 5 Quantification of **a** Fe-based IMC particles Area fraction, size, and circularity analyzed from BSE images and **b** Number density (count per µm^2), size (nm), and circularity of nano-sized dispersoid precipitates analyzed from STEM HAADF images at various Fe content

analysis was performed over the whole cross-sections of all samples at a randomly selected area as shown in inverse pole figure (IPF) maps of the X-axis (Extrusion Direction—ED) in Fig. 7. It is noticeable that the grain structure consists of a peripheral recrystallized coarse grain (PCG) at the surface, a subsurface fibrous grain structure (denoted by green color), and central fibrous region (purple combination) (Fig. 7a–c). A fibrous grain structure at the centre of profile thickness possesses a combination of 4 texture components known as *β-fibre*. For fibrous alloys, the influence of Fe is not straightforward from the images, therefore complementing the analysis with the fraction of texture components will be performed.

To further discuss the evolution of texture for each specific region of the longitudinal cross-section (Fig. 8), a representative orientation distribution function (ODF) map was obtained and presented in Fig. 6 at 0.2Fe conditions. For the quantification of texture components analysis of ODF maps was carried out by the FCC texture components that are summarized in Table 1.

According to the ODF data, the centre of thickness follows a β-fibre texture where all components of Brass (Fig. 8a at φ_2 0°), Copper (Fig. 8a φ_2 45°) and S (Fig. 8a φ_2 60°) contribute to the central fibrous region. The recrystallization Cube component appears to be present as shown in Fig. 8a φ_2 0° which has also been reported by Goik et al. in fibrous AA6082 [12]. At the subsurface parts of the alloy,

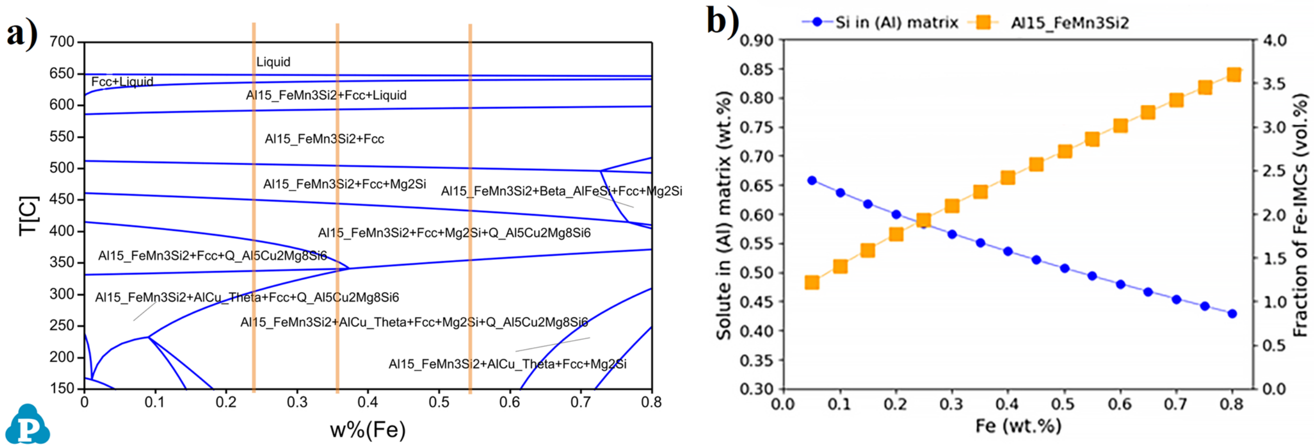

Fig. 6 Thermodynamic **a** pseudo-binary phase diagram calculations versus Fe content with **b** solute Si and Fe-based IMCs phase fraction calculations by changing Fe content

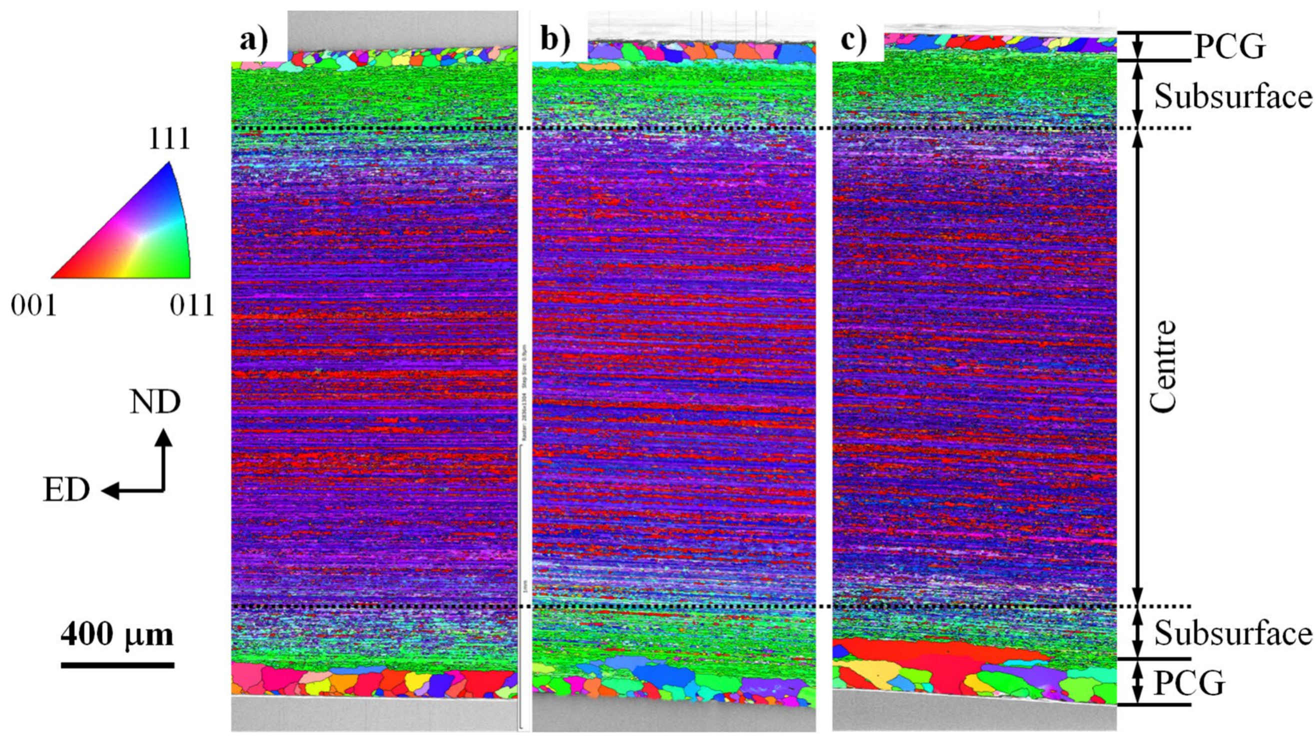

Fig. 7 EBSD IPF maps at **a** 0.2Fe, **b** 0.3Fe, and **c** 0.5Fe taken from the side of the profiles where the extrusion direction is parallel to the X-axis. All images are at same magnification

the β-fibre texture disappears gradually, and B-fibre starts to appear as shown in Fig. 8b φ_2 45°. The PCG at the surface of the extrudate also has a component of the Goss and Goss/Brass (Fig. 8c).

To explain the effect of iron addition on the microstructure and properties, each of the component fractions was calculated based on the texture components obtained from the EBSD maps (Fig. 7) and plotted in Fig. 9. It is evident that all components of the *β-fibre* contribute to the fibrous region at the centre of the extruded profile considering that the distribution of each component depends on the activation of slip systems during deformation. Hirsch has stated that in aluminium alloys containing very low amount of constituent elements, the stacking fault energy is relatively high, and the twinning rarely takes place [64]. From the perspective of alloying elements, Cu addition in aluminium has been shown to increase SFE while Mg reduces the SFE as in the AA5xxx series [41, 42, 65]. However, in the present study the individual additions of Mg, Si and Cu elements are less than those in AA5xxx series. The addition of Fe up to

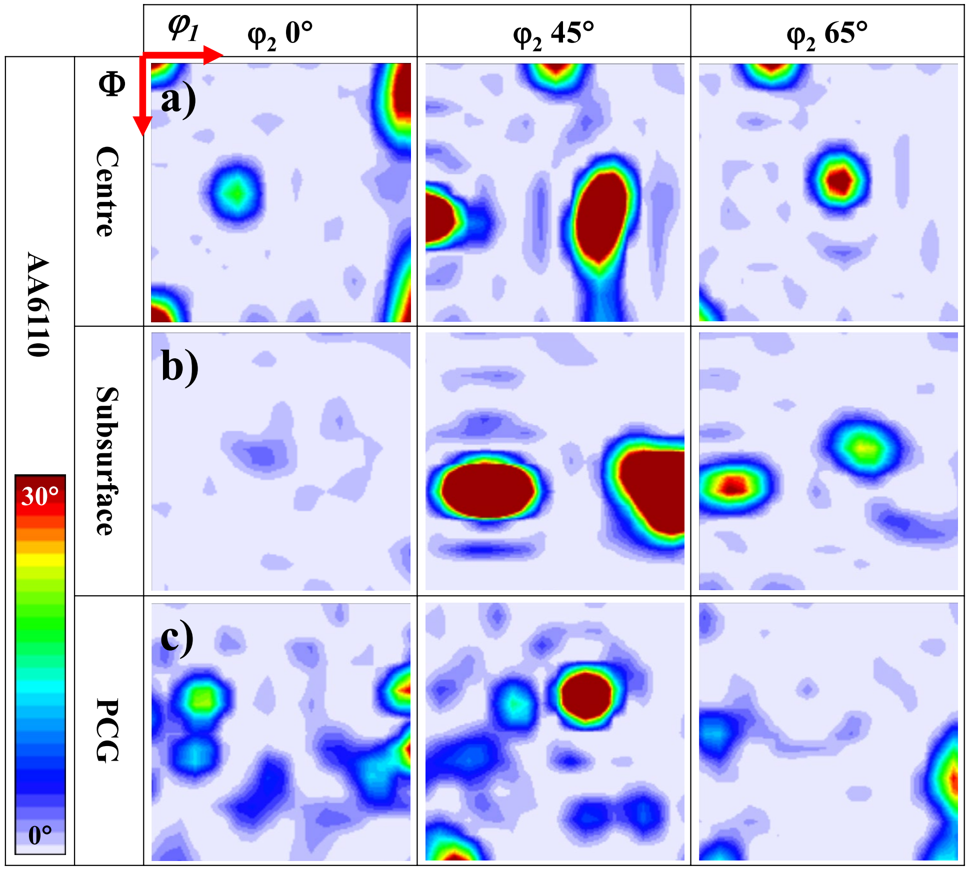

Fig. 8 ODF maps calculated from each part of EBSD maps shown in Fig. 7 at **a** centre of thickness, **b** subsurface, and **c** PCG surface

Table 1 Various texture component names with respect to each corresponding Euler Angles

Texture Component		Orientation	Euler angles		
			φ_1	Φ	φ_2
Recrystallization fibre	Cube	$\{001\} \parallel \langle 100\rangle$; $\langle 100\rangle \parallel ED$	0/90	0	0/90
β-fibre	Goss	$\{011\} \parallel \langle 100\rangle$	0	45	0/90
	Brass	$\{011\} \parallel \langle 211\rangle$	35	45	0/90
			54	90	45
	S	$\{123\} \parallel \langle 634\rangle$	59	37	63
			52	74	33
			27	57	18
	Copper	$\{112\} \parallel \langle 111\rangle$	90	35	45
			39	65	26
B-fibre	B	$\{\bar{1}12\} \parallel \langle 110\rangle$; $\langle 110\rangle \parallel ED$	0	55	45
	$\overline{\mathrm{B}}$	$\{1\bar{1}\bar{2}\} \parallel \langle\bar{1}\bar{1}0\rangle$	60	55	45

the level of 0.7 wt% is believed not to change the SFE due to poor solubility and the aluminium is still the dominant element determining the SFE.

Grain size refinement is another consequence of Fe addition as shown in Fig. 10a as the area fraction of large grains (over 200 μm) is less frequent by increasing Fe content (e.g. 0.5Fe). The area-weighted average grain size data was measured from EBSD results based on ASTM E2627 considering HAGB ≥ 10°. Based on the average grain size values in Fig. 10, it is evident that the grain refinement has occurred in the centre part. The mechanism of grain refinement via iron IMCs has been explained by Wang et al. [66]. They mentioned that particles having a diameter of more than 1 μm, mostly α-Al(FeMn)Si IMCs, have the potential to act as substrates for recrystallization utilizing PSN [47]. One should point out the difference between dispersoids in pinning GBs with IMCs in grain refinement. According to Nes [67], the wrought microstructure contains two dominating structural particles within the matrix: the bimodal coarse particles (i.e. micro-sized Al(Fe,Mn)Si IMCs and coarse Mg_2Si particles; and fine particles (i.e. nano-sized Al(Fe,Mn)Si and Mg_2Si precipitates). The micro-sized particles promote recrystallization through PSN that are recognised as the increment of the stored energy in the deformation zone around them. Conversely, the nano-sized particles impede recrystallization process by exerting a Zener pinning force [28, 68]. The Zener pinning force offsets the driving force of recrystallization while stored energy because of plastic deformation enhances the recrystallization. This balance determines the microstructure of the material after deformation.

The grain refinement as a result of Fe addition in hot extrusion of the AA6110 fibrous alloy is an indication of

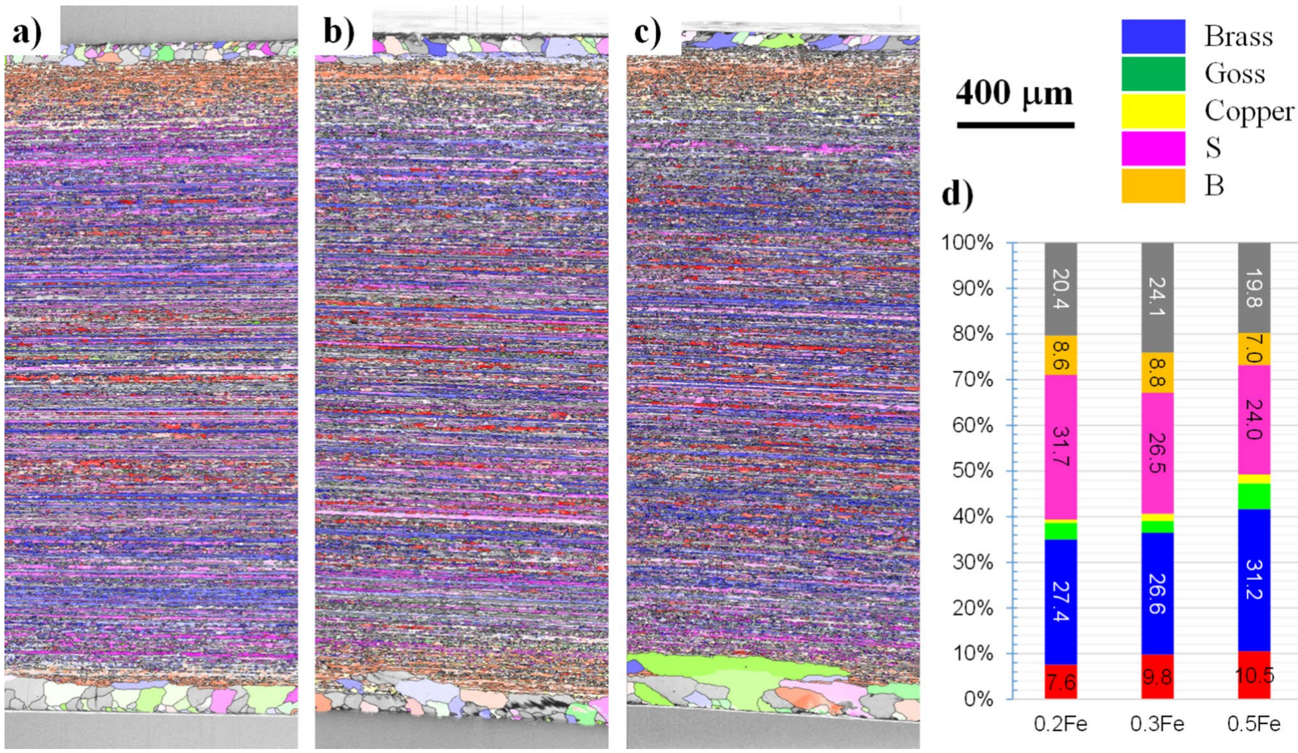

Fig. 9 Texture components distribution map obtained from EBSD data at **a** 0.2Fe, **b** 0.3Fe, **c** 0.5Fe with d) quantitative fraction. All images have the same magnification

manipulation of dynamic recrystallization during high temperature deformation. This was further elaborated via looking into the misorientation angle distribution obtained from the fibrous region of Fig. 7 and plotted in Fig. 10b. It can be inferred that the misorientation angle frequency of all samples has two distinctly separated peaks at low angle (5°) and at high angle (58°). The HAGBs are showing and increasing frequency by increasing Fe content (from 0.2Fe-red to 0.3Fe-green and 0.5Fe-blue) which is an indication of increasing higher fraction of HAGB leading to a finer grain size. This is an indication of facilitating recrystallization through PSN which will be discussed further.

B-fibre is reported to take place in severe plastic deformation (SPD) processes such as equal channel angular pressing (ECAP) and high-pressure torsion (HPT) [12, 69–72]. Here, in the extrusion process, the friction due to the contact between the die and the material during the extrusion process results in the shear deformation of the Al matrix at the contact zone with the extrusion die. Based on experimental results and finite element modelling, Mahmoodkhani et al. have studied the surface grain structure during extrusion. The authors concluded that the shear component can be controlled via die geometry management [73–75]. The formation of B texture shown in EBSD IPF map of Fig. 11a as a result of die shear has a direct correlation with the formation of equiaxed PCG grains. In fibrous alloys, this can be prevented by using a choke bearing at the die bearing. Similar observations were separately reported by Goik et al. [12] and Chen et al. [71]. According to Negozio et al. [57] the mechanism of PCG occurrence depends on simultaneous existence of high DRX, high temperature, and high strain rate. Wherever satisfied (mostly at the surface where shear strain exists and temperature exceeds rapidly), the driving force for recrystallization surpasses the Zener pressure retarding force and equiaxed grain nucleate and grows. If conditions are met, Goik et al. have demonstrated [12] that the equiaxed PCG grains tend to consume all B texture shear grains from a crystallographic viewpoint. As indicated by black arrows in Fig. 11b–d, there's a close correlation between {110} planes of PCG and shear textured grains). Thus, the reason that prevents PCG grain growth lies in the inhibition of grain boundary migration because of increasing number density of dispersoid precipitation as shown in Figs. 4 and 5b.

The presence of Fe-rich IMCs has an impact on grain structure by decreasing grain size in the bulk structure as reported earlier in Fig. 10. To observe the effect of Fe-based IMCs on grain refinement, a simultaneous EBSD/EDS map was obtained from 0.5Fe condition in the fibrous region, as shown in Fig. 12. Enrichment of Fe, Si, and Mn (Fig. 12c–e) accompany the presence of IMCs (red colour areas in Fig. 12a). According to the IPF map in Fig. 12b, the IMC

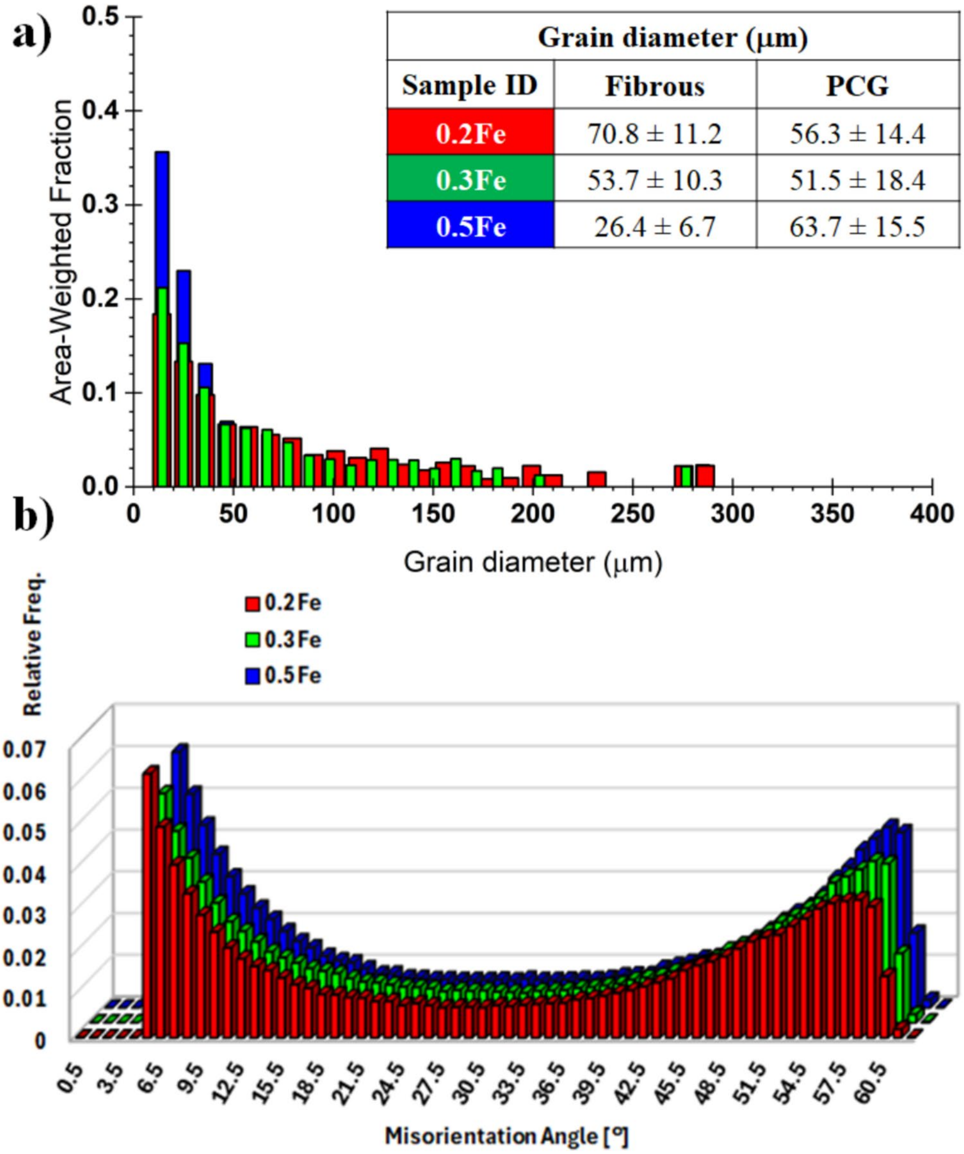

Fig. 10 Statistical **a** grain size in quantitative numeric with average weighted fraction and **b** misorientation angle distribution obtained from EBSD data in Fig. 7 fibrous region

particles are surrounded by tiny grains within 2–5 µm size range, which have an orientation different from the typical ⟨111⟩ and ⟨001⟩ seen in fibrous microstructures, as indicated by yellow arrows. Dynamic recrystallization was reported to take place during high-temperature extrusion of an Al–Mg-Si alloy as presented by Zhang et al. [7]. Therefore, recrystallization due to PSN can also occur by dynamically after high residual strain is being imposed to the surrounding matrix by IMC particles [76–79].

3.2 Effect of Fe on Mechanical Properties

The tensile properties shown in Fig. 13a, c show a slight reduction in yield strength (TYS) as well as ultimate tensile strength (UTS) by increasing iron content. The effect of iron in AA6xxx series has already been well-established [16]. On one side, it has a high tendency to consume Si by forming β (in cast structure) and α-AlFeSi (after homogenisation treatment) IMCs. Since Si provides a strengthening effect in both its solid solution and through the formation of Mg_2Si precipitates, reducing free Si will result in a reduction of precipitation hardening. This was proven via thermodynamic phase fraction calculation in Fig. 6b. Additionally, the formation of IMC particles has been said to affect mechanical properties by resisting deformation while the surrounding matrix deforms easily. The result is the formation of cracks from the broken IMC particles [34, 44, 80, 81].

Bendability versus tensile properties is a valuable comparison for assessing the ductility of an engineering material for automotive applications. Since the bendability of the material depends on the surface characteristics of the grains, PCG thickness and texture components of the peripheral grains are important. In AA6110 having a hybrid grain structure (e.g. fibrous and recrystallized PCG), various

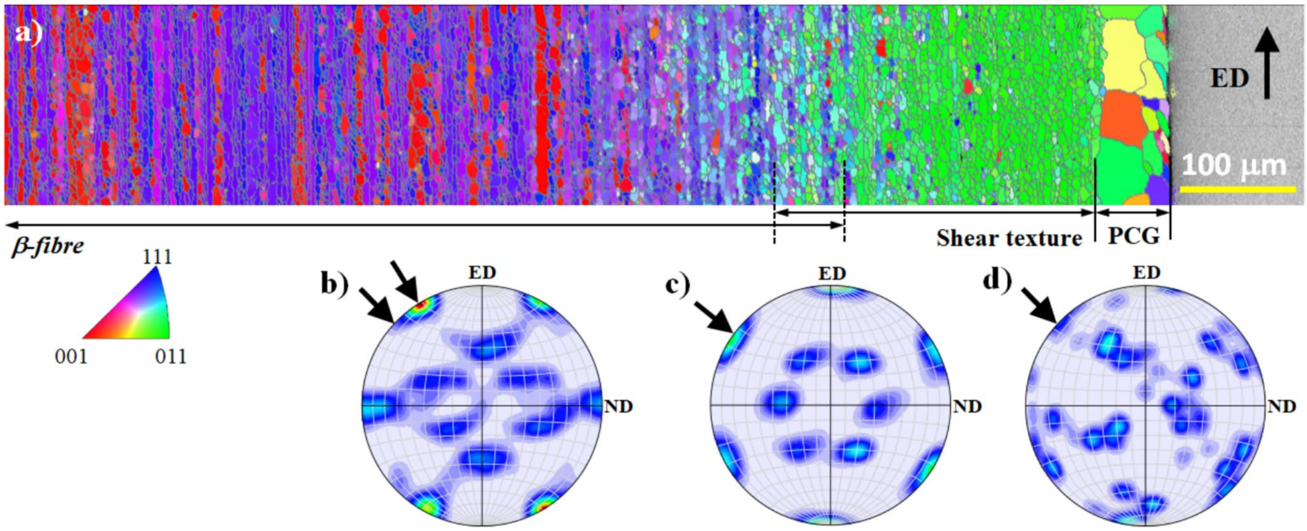

Fig. 11 **a)** EBSD IPF map of surface to the centre of thickness distinguishing three layers of equiaxed PCG, fibrous shear texture at the subsurface accompanied by corresponding PF of **b**) β-fibre, **c)** B shear texture, and **d)** PCG gradually emerging toward the centre of thickness

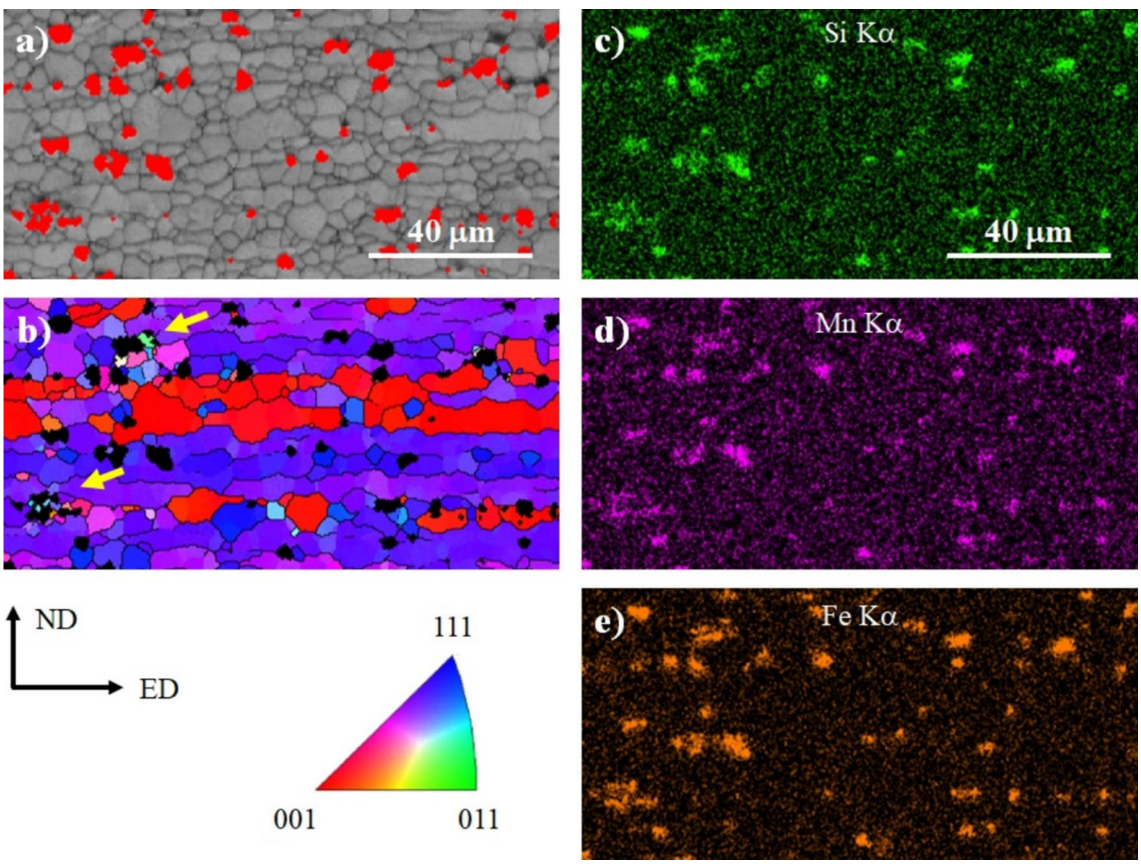

Fig. 12 Observation of grain refinement around the Fe-based IMCs via EBSD **a** Phase map and **b** IPF on Al matrix excluding IMC particles and EDS **c** Si Kα, **d** Mn Kα, and **e** Fe Kα mapping

parameters affect the bendability of the material such as PCG thickness, hardening behavior, anisotropy, and alignment of IMC particles [82]. Our observations on Fig. 13b show that by increasing the Fe content, the bending angle of the material increases slightly while experiencing a tensile strength decrease. As presented in Fig. 2, increasing Fe content reduces PCG thickness. The mechanism for mechanical properties dependence to increasing Fe content can be

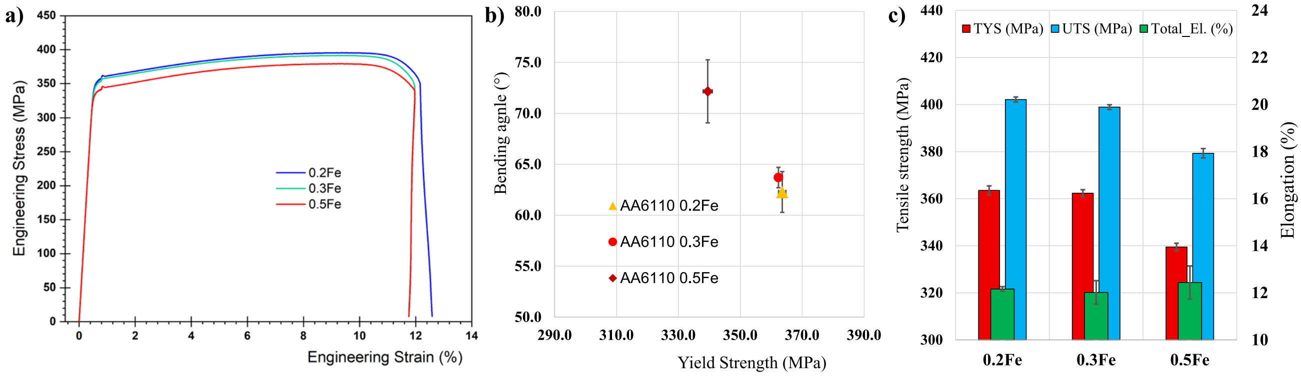

Fig. 13 Result of mechanical **a** tensile yield, ultimate strength, and total elongation and **b** bending angle versus tensile yield strength having different Fe contents

attributed to different factors. Firstly, an enhanced level of α-Al(FeMn)Si IMCs by increasing iron as shown in Fig. 3, quantitatively measured in Fig. 5a, and thermodynamically calculated in Fig. 6. The IMC particles consume more Si resulting in less strengthening precipitates formation (*i.e.* Mg_2Si) [62, 63]. Secondly, the addition of iron not only increases the number density of IMCs but also enhances the precipitation of nano-sized dispersoid particles as presented in Fig. 4 and quantitatively measured in Fig. 5b. The dispersoid particles prevent grain migration by increasing Zener pressure proposed by Zener [83] and explained by Liu et al. [84]. The result is inhibition of recrystallization and grain growth from the peripheral grains that were demonstrated on EBSD IPF map of Fig. 11. Conclusively, the PCG thickness reduces by increasing Fe content. Thirdly, Elasheri et al. [82] have elucidated the relationship between surface characteristics of AA6xxx extrudate profiles such as PCG thickness and bending properties and concluded that the thickness of the PCG layer has a direct correlation with bending angle. Due to the undesirable recrystallization texture that was observed at peripheral grains (as shown in Fig. 9), cannot tolerate tension and compression on either side of the surface during bending resulting in loss of ductility and formation of crack that propagates through thickness.

Engineering stress–strain curves have shown a profound plastic deformation prior to fracture in all alloys (Fig. 13a). after UTS, the localized necking has led to a reduction in thickness followed by a swift propagation of crack. Assuming that all samples follow the same fracture mode, one example of fracture surface at 0.5Fe was observed under electron microscope for further examination and presented in Fig. 14. From Fig. 14a, we can witness a 45° inclination of fracture surface with respect to the applied load direction. This is because although tensile load was applied horizontally, the material experiences maximum shear on the planes at ± 45° activated by the FCC slip system [85, 86]. At the periphery, intergranular (IG) fracture was observed where crack follows grain boundary regardless of IMC trace path as shown in Fig. 14c, f. The reason was explained to be due to the GB decohesion. At the central fibrous region; however, the IMC network dominates the path of crack tip growth as shown on the cross-section at Fig. 14b and top fracture surface in Fig. 14e.

Further analysis was performed on the bending samples using optical microscopy on the anodized samples. Figure 15 shows the overall grain structure of the bent samples. It's evident that the deformation has led to the curvature of fibrous during deformation. The cracking that has sheared through the fibers can also be observed in 0.5Fe condition (Fig. 15c).

To further analyze the microstructure of bending tested samples, one sample from maximum Fe content was analyzed by low magnification EBSD to observe the grain structure in Fig. 16. Band contrast (BC) image (Fig. 16a) clearly demonstrates the abundance of deformation at both the compression and tension sides of the bent samples. Shear band formation is the response of the material to relaxing after further deformation [87]. The accumulation of shear bands followed by further applying deformation is the most suitable position for crack growth and failure [82]. In addition, the grain boundaries possessing IMC particles are also prone to void formation as a result of boundary decohesion [88]. This might be the reason for the start of crack formation and propagation from the coarse surface grains (PCG) in the form of intergranular fracture.

A comparison of residual strains from the GND map in Fig. 16c clearly justifies that the fibrous structure is capable of withstanding deformation by distributing the applied stress throughout the whole microstructure. Furthermore, the crystallography of each grain with respect to applied stress is responsible for activation of slip system to further tolerate the deformation. Comparing GND maps in Fig. 16 and IPF maps in Fig. 7, it can be inferred that the PCG

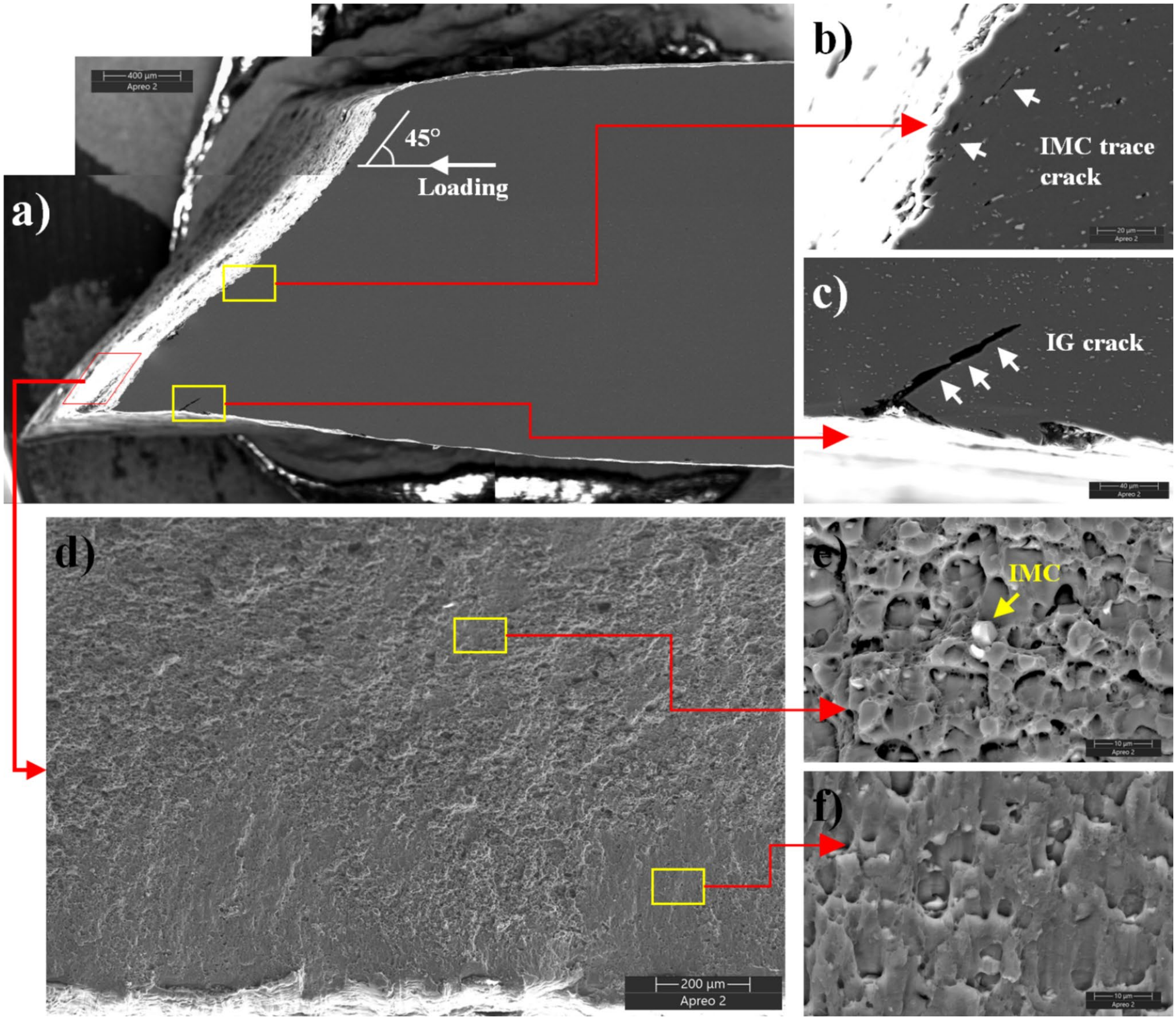

Fig. 14 Fracture surface analysis of the 0.5Fe tensile tested sample from **a**, **b**, **c** cross-section side view and **d**, **e**, **f** top fracture surface

grains are less tolerant to applying deformation relative to the fibrous structure acting as an initiation of failure during bending.

In conclusion, Fe impurity addition to AA6110 extrusion alloys can lead to a set of complex effects. It is obvious that the entrapment of part of the Si content in IMC particles leads to a decrease in precipitation hardening. Increasing iron content reduces PCG thickness which affects bendability of the alloy. The IMC particles also act as nucleation site for newly recrystallized small grains having a texture far from β-fibre. When comparing recrystallized alloys with fibrous alloys, one can conclude that the nature of Cube texture has been known to have lower strength and high ductility. The Fe addition in recrystallized AA6008 has increased the total IMC content. PSN has led to grain refinement in equi-axed grain structure, too. From the perspective of mechanical properties, a reduction in tensile properties have been similarly observed in recrystallized alloy, too. On the other hand, bendability of the recrystallized alloys has observed to decrease by increasing Fe content. It was found that the reason is due to the modification of the PCG layer in recrystallized alloys (proved by EBSD texture components) where intergranular crack nucleates from the surface and propagates towards the thickness. Whereas the bendability was slightly improved in fibrous alloys mainly due to a decrease in thickness of PCG layer where crack is nucleated from the surface but hinders in fibrous region.

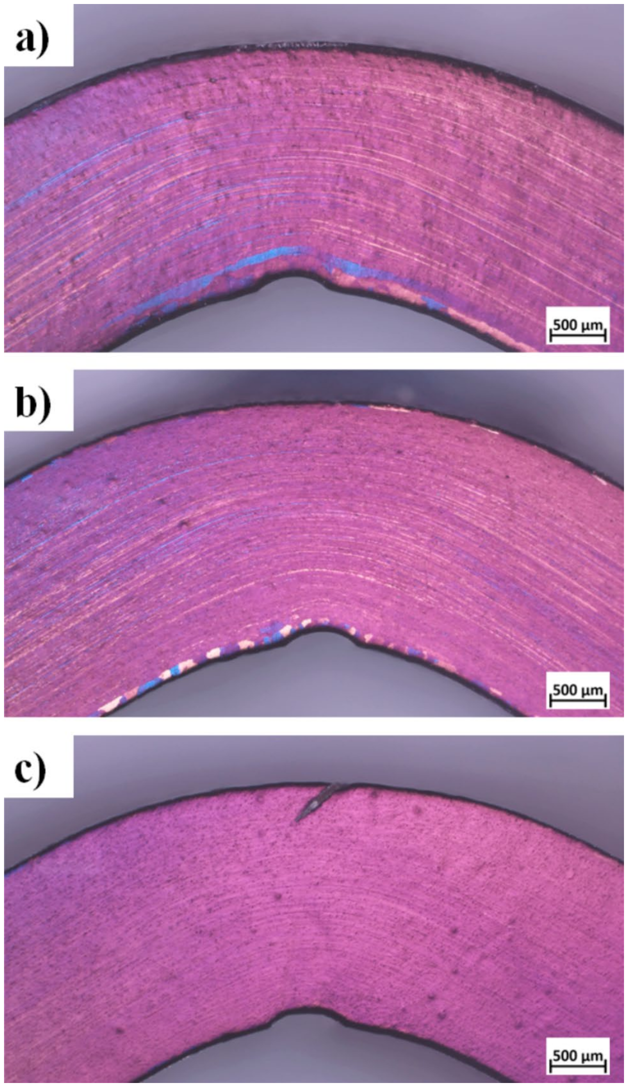

Fig. 15 Optical microscopy anodized images of bent samples at **a** 0.2Fe, **b** 0.3Fe, and **c** 0.5Fe Fe content

4 Conclusions

In this paper, the effect of single impurity Fe addition on the AA6110 fibrous alloy was investigated from the viewpoint of microstructural and mechanical properties. The extruded flat strip profiles were analyzed by optical and electron microscopy before and after bending tests and following conclusions were made:

- The Fe addition increases the area fraction and size of the α-Al(Fe,Mn)Si intermetallic particles while it does not affect their morphology proven by thermodynamic calculation and image analysis.
- The β-fibre texture is dominant in the fibrous region accompanied by a layer of B-fibre shear texture at subsurface and PCG grains at the surface.
- The thickness of peripheral coarse grains (PCG) is found to decrease by increasing Fe content in this alloy due to increasing the fraction of nano-sized dispersoid particles which inhibit grain growth.
- Increased Fe content increases the Fe-based IMC area fraction and number density of dispersoid precipitates while reducing the free solute Si. However, it does not alter the tensile strength and bending properties drastically. Thus, the alloy is capable of maintaining the required properties despite additional Fe content.

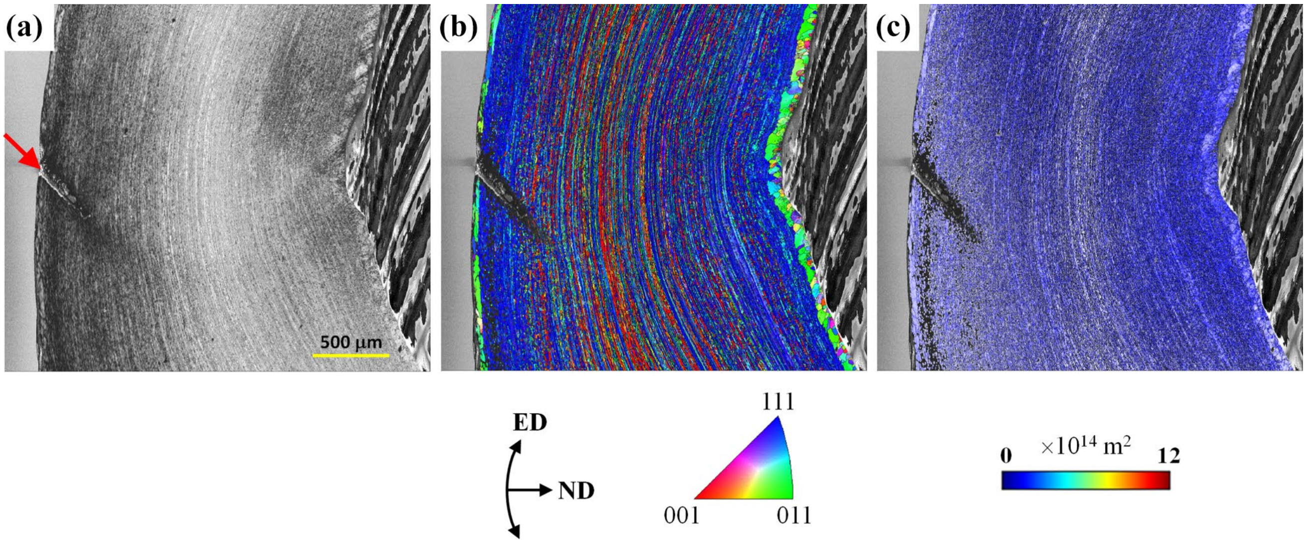

Fig. 16 EBSD low magnification **a** BC, **b** IPF at TD (Z-axis), and **c** GND maps of bending tested sample at 0.5Fe condition

Acknowledgements The author would like to appreciate help and support from Constellium, UK.

Funding This work was not supported by any project.

Data Availability Data is available upon a reasonable request from the corresponding author.

Declarations

Competing interests The authors declare that they have no known competing financial interests or personal relationships that could have appeared to influence the work reported in this paper.

References

1. T. Sheppard, Metallurgical features affecting the extrusion of aluminium alloys BT - Extrusion of Aluminium Alloys, in: T. Sheppard (Ed.), Springer US, Boston, MA, 1999: pp. 69–126. https://doi.org/10.1007/978-1-4757-3001-2_3.
2. W.S. Miller, L. Zhuang, J. Bottema, A.J. Wittebrood, P. De Smet, A. Haszler, A. Vieregge, Recent development in aluminium alloys for the automotive industry. Mater. Sci. Eng. A **280**, 37–49 (2000). https://doi.org/10.1016/S0921-5093(99)00653-X
3. E. Georgantzia, M. Gkantou, G.S. Kamaris, Aluminium alloys as structural material: a review of research. Eng. Struct. **227**, 111372 (2021). https://doi.org/10.1016/j.engstruct.2020.111372
4. A.P. Sekhar, A. Samaddar, A.B. Mandal, D. Das, Influence of ageing on the intergranular corrosion of an Al–Mg–Si alloy. Met. Mater. Int. **27**, 5059–5073 (2021). https://doi.org/10.1007/s12540-020-00843-1
5. Z. Yang, J. Tang, X. Mo, W. Chen, D. Fu, H. Zhang, J. Teng, F. Jiang, Microstructure, mechanical properties, and strengthening mechanisms of ultra-high strength Al-Zn-Mg-Cu alloy prepared by continuous extrusion forming process. Mater. Des. **242**, 112985 (2024). https://doi.org/10.1016/j.matdes.2024.112985
6. S. Karabay, M. Yilmaz, M. Zeren, Investigation of extrusion ratio effect on mechanical behaviour of extruded alloy AA-6101 from the billets homogenised-rapid quenched and as-cast conditions. J. Mater. Process. Technol. **160**, 138–147 (2005). https://doi.org/10.1016/j.jmatprotec.2004.05.025
7. C. Zhang, C. Wang, Q. Zhang, G. Zhao, L. Chen, Influence of extrusion parameters on microstructure, texture, and second-phase particles in an Al-Mg-Si alloy. J. Mater. Process. Technol. **270**, 323–334 (2019). https://doi.org/10.1016/j.jmatprotec.2019.03.014
8. Y. Zhao, B. Song, J. Pei, C. Jia, B. Li, G. Linlin, Effect of deformation speed on the microstructure and mechanical properties of AA6063 during continuous extrusion process. J. Mater. Process. Technol. **213**, 1855–1863 (2013). https://doi.org/10.1016/j.jmatprotec.2013.05.006
9. T. Homma, T. Honma, D. Terada, M. Hoshino, Effects of extrusion speed and compounds on surface defects in extruded-AA7003 alloy. Mater. Sci. Technol. (United Kingdom) **37**, 785–793 (2021). https://doi.org/10.1080/02670836.2021.1949855
10. A. Aytaç, B. Daşçilar, M. Usta, The effect of extrusion speed on the structure and corrosion properties of aged and non-aged 6063 aluminum alloy. Mater. Chem. Phys. **130**, 1357–1360 (2011). https://doi.org/10.1016/j.matchemphys.2011.09.029
11. R. Lu, S. Zheng, J. Teng, J. Hu, D. Fu, J. Chen, G. Zhao, F. Jiang, H. Zhang, Microstructure, mechanical properties and deformation characteristics of Al-Mg-Si alloys processed by a continuous expansion extrusion approach. J. Mater. Sci. Technol. **80**, 150–162 (2021). https://doi.org/10.1016/j.jmst.2020.11.055
12. P. Goik, A. Schiffl, H.W. Höppel, Formation of peripheral coarse grain in thin-walled Al–Mg–Si extrusion profiles. Metall. Mater.

Trans. A **54**, 3940–3956 (2023). https://doi.org/10.1007/s11661-023-07144-3
13. D. Yin, Q. Xiao, Y. Chen, H. Liu, D. Yi, B. Wang, S. Pan, Effect of natural ageing and pre-straining on the hardening behaviour and microstructural response during artificial ageing of an Al-Mg-Si-Cu alloy. Mater. Des. **95**, 329–339 (2016). https://doi.org/10.1016/j.matdes.2016.01.119
14. H. Jin, D. Tie, R. Guan, Precipitation behavior during re-aging of Al-Mg-Si-Cu alloy. Mater. Des. **220**, 110883 (2022). https://doi.org/10.1016/j.matdes.2022.110883
15. D. Kim, H. Maeng, Y. Choi, H. Choi, S.J. Lee, Constitutive model of triple-step-aged Al–Mg–Si alloy incorporating precipitation kinetics. Met. Mater. Int. **27**, 4577–4585 (2021). https://doi.org/10.1007/s12540-020-00845-z
16. T. Sheppard, Processing of 6XXX alloys BT - Extrusion of Aluminium Alloys, in: T. Sheppard (Ed.), Springer US, Boston, MA, 1999: pp. 253–322. https://doi.org/10.1007/978-1-4757-3001-2_6.
17. Y. Birol, Effect of Cr and Zr on the grain structure of extruded en AW 6082 alloy. Met. Mater. Int. **20**, 727–732 (2014). https://doi.org/10.1007/s12540-014-4018-x
18. S.I. Park, H.M. Lee, Alloy design of intermetallic dispersion strengthened aluminum systems by mechanical alloying for high temperature applications. Met. Mater. **6**, 17–24 (2000). https://doi.org/10.1007/BF03026340
19. D.H. Lee, S.W. Nam, Role of Mn-dispersoid in the fracture toughness enhancement of Al–Zn–Mg–(Mn) alloys. Met. Mater. **1**, 71–76 (1995). https://doi.org/10.1007/BF03055326
20. A. Elasheri, A. Ghosh, N. Parson, X.G. Chen, Microstructure and texture evolution during extrusion of 6xxx aluminum alloys with Mn/Zr additions. J. Mater. Sci. **60**, 22252–22269 (2025). https://doi.org/10.1007/s10853-025-11646-3
21. K. Liu, X.-G. Chen, Development of Al–Mn–Mg 3004 alloy for applications at elevated temperature via dispersoid strengthening. Mater. Des. **84**, 340–350 (2015)
22. A.R. Farkoosh, X.G. Chen, M. Pekguleryuz, Dispersoid strengthening of a high temperature Al–Si–Cu–Mg alloy via Mo addition. Mater. Sci. Eng. A **620**, 181–189 (2015)
23. K. Liu, H. Ma, X.-G. Chen, Enhanced elevated-temperature properties via Mo addition in Al–Mn–Mg 3004 alloy. J. Alloys Compd. **694**, 354–365 (2017)
24. Z. Li, Z. Zhang, X.-G. Chen, Microstructure, elevated-temperature mechanical properties and creep resistance of dispersoid-strengthened Al–Mn–Mg 3xxx alloys with varying Mg and Si contents. Mater. Sci. Eng. A **708**, 383–394 (2017)
25. Y.J. Li, W.Z. Zhang, K. Marthinsen, Precipitation crystallography of plate-shaped Al6 (Mn, Fe) dispersoids in AA5182 alloy. Acta Mater. **60**, 5963–5974 (2012)
26. R. Zhang, Y. Zhang, Y. Yan, S. Thomas, C.H.J. Davies, N. Birbilis, The effect of reversion heat treatment on the degree of sensitisation for aluminium alloy AA5083. Corros. Sci. **126**, 324–333 (2017)
27. C.L. Liu, Q. Du, N.C. Parson, W.J. Poole, The interaction between Mn and Fe on the precipitation of Mn/Fe dispersoids in Al-Mg-Si-Mn-Fe alloys. Scr. Mater. **152**, 59–63 (2018)
28. X. Qian, N. Parson, X.G. Chen, Effects of Mn addition and related Mn-containing dispersoids on the hot deformation behavior of 6082 aluminum alloys. Mater. Sci. Eng. A **764**, 138253 (2019). https://doi.org/10.1016/j.msea.2019.138253
29. S.W. Nam, D.H. Lee, The effect of Mn on the mechanical behavior of Al alloys. Met. Mater. **6**, 13–16 (2000). https://doi.org/10.1007/BF03026339
30. Z. Que, Y. Wang, C.L. Mendis, C. Fang, J. Xia, X. Zhou, Z. Fan, Understanding Fe-containing intermetallic compounds in Al alloys: an overview of recent advances from the LiME research hub. Metals (2022). https://doi.org/10.3390/met12101677
31. Z. Que, Y. Wang, Z. Fan, Formation of the Fe-containing intermetallic compounds during solidification of Al–5Mg–2Si–0.7Mn–1.1Fe alloy. Metall. Mater. Trans. A **49**, 2173–2181 (2018). https://doi.org/10.1007/s11661-018-4591-6
32. Y. Wu, H. Liao, J. Yang, K. Zhou, Effect of Si content on dynamic recrystallization of Al-Si-Mg alloys during hot extrusion. J. Mater. Sci. Technol. **30**, 1271–1277 (2014). https://doi.org/10.1016/j.jmst.2014.07.011
33. L.H. Pereira, G.H. Asato, L.B. Otani, A.M. Jorge, C.S. Kiminami, C. Bolfarini, W.J. Botta, Changing the solidification sequence and the morphology of iron-containing intermetallic phases in AA6061 aluminum alloy processed by spray forming. Mater Charact **145**, 507–515 (2018). https://doi.org/10.1016/j.matchar.2018.09.006
34. S. Ji, W. Yang, F. Gao, D. Watson, Z. Fan, Effect of iron on the microstructure and mechanical property of Al–Mg–Si–Mn and Al–Mg–Si diecast alloys. Mater. Sci. Eng. A **564**, 130–139 (2013)
35. X. Dong, X. Zhu, S. Ji, Effect of super vacuum assisted high pressure die casting on the repeatability of mechanical properties of Al-Si-Mg-Mn die-cast alloys. J. Mater. Process. Technol. **266**, 105–113 (2019)
36. P. Zhang, Z. Li, B. Liu, W. Ding, L. Peng, Improved tensile properties of a new aluminum alloy for high pressure die casting. Mater. Sci. Eng. A **651**, 376–390 (2016)
37. A.M. Cassell, J.D. Robson, C.P. Race, A. Eggeman, T. Hashimoto, M. Besel, Dispersoid composition in zirconium containing Al–Zn–Mg–Cu (AA7010) aluminium alloy. Acta Mater. **169**, 135–146 (2019). https://doi.org/10.1016/j.actamat.2019.02.047
38. E.M. Elgallad, K. Liu, Z. Zhang, X.G. Chen, Effect of transition elements on dispersoid formation and elevated-temperature mechanical properties in 6082 aluminum alloy. Philos. Mag. **101**, 96–116 (2021). https://doi.org/10.1080/14786435.2020.1826592
39. F. Sadeghi, T. Zargar, J.W. Kim, Y.-U. Heo, J.S. Lee, C.H. Yim, The effect of Ni depletion on athermal martensitic transformation in 304 austenitic stainless steel. Mater Charact **175**, 111063 (2021). https://doi.org/10.1016/j.matchar.2021.111063
40. F. Sadeghi, T. Zargar, J.W. Kim, Y.U. Heo, J.S. Lee, C.H. Yim, Role of the annealing twin boundary on the athermal α′-martensite formation in a 304 austenitic stainless steel. Materialia **20**, 101218 (2021). https://doi.org/10.1016/j.mtla.2021.101218
41. Y.Z. Tian, L.J. Zhao, N. Park, R. Liu, P. Zhang, Z.J. Zhang, A. Shibata, Z.F. Zhang, N. Tsuji, Revealing the deformation mechanisms of Cu–Al alloys with high strength and good ductility. Acta Mater. **110**, 61–72 (2016). https://doi.org/10.1016/j.actamat.2016.03.015
42. N.M. Chavan, P.S. Phani, M. Ramakrishna, L. Venkatesh, P. Pant, G. Sundararajan, Role of stacking fault energy (SFE) on the high strain rate deformation of cold sprayed Cu and Cu–Al alloy coatings. Mater. Sci. Eng. A **814**, 141242 (2021). https://doi.org/10.1016/j.msea.2021.141242
43. H. Zhong, P.A. Rometsch, Y. Estrin, The influence of Si and Mg content on the microstructure, tensile ductility, and stretch formability of 6xxx alloys. Metall. Mater. Trans. A **44**, 3970–3983 (2013). https://doi.org/10.1007/s11661-013-1740-9
44. J.A. Österreicher, A.R. Arnoldt, S. Gneiger, G. Kunschert, Tolerance of Al–Mg–Si wrought alloys for high Fe contents: the role of effective Si. Metall. Mater. Trans. A **54**, 4472–4480 (2023). https://doi.org/10.1007/s11661-023-07180-z
45. S. Kumar, P.S. Grant, K.A.Q. O'Reilly, Evolution of Fe bearing intermetallics during DC casting and homogenization of an Al-Mg-Si Al alloy. Metall. Mater. Trans. A **47**, 3000–3014 (2016). https://doi.org/10.1007/s11661-016-3451-5
46. S. Kumar, K.A.Q. O'Reilly, Influence of Al grain structure on Fe bearing intermetallics during DC casting of an Al–Mg–Si alloy. Mater Charact **120**, 311–322 (2016). https://doi.org/10.1016/j.matchar.2016.09.017

47. S. Hovden, J. Kronsteiner, A. Arnoldt, D. Horwatitsch, G. Kunschert, J.A. Österreicher, Parameter study of extrusion simulation and grain structure prediction for 6xxx alloys with varied Fe content. Mater. Today Commun. **38**, 108128 (2024). https://doi.org/10.1016/j.mtcomm.2024.108128
48. F.J. Humphreys, M. Hatherly, Recrystallization and related annealing phenomena, elsevier, 2012.
49. R. Kumar, N. Ansari, T.R. Dandekar, R.K. Khatirkar, Correlation of microstructure, texture and intermetallic particles during multi-step cross-rolling and annealing in a strip-cast AA8011 alloy. Mater. Today Commun. **35**, 105812 (2023). https://doi.org/10.1016/j.mtcomm.2023.105812
50. J.-H. Ryu, D.N. Lee, The effect of precipitation on the evolution of recrystallization texture in AA8011 aluminum alloy sheet. Mater. Sci. Eng. A **336**, 225–232 (2002)
51. H. She, D. Shu, A. Dong, J. Wang, B. Sun, H. Lai, Relationship of particle stimulated nucleation, recrystallization and mechanical properties responding to Fe and Si contents in hot-extruded 7055 aluminum alloys. J. Mater. Sci. Technol. **35**, 2570–2581 (2019). https://doi.org/10.1016/j.jmst.2019.07.014
52. V. Aryshenskii, F. Grechnikov, E. Aryshenskii, Y. Erisov, S. Konovalov, M. Tepterev, A. Kuzin, Alloying elements effect on the recrystallization process in magnesium-rich aluminum alloy. Materials (2022). https://doi.org/10.3390/ma15207062
53. J. Liu, D. Kaoumi, Use of in-situ TEM to characterize the deformation-induced martensitic transformation in 304 stainless steel at cryogenic temperature. Mater Charact **136**, 331–336 (2018). https://doi.org/10.1016/j.matchar.2017.12.005
54. N.M. Siddesh Kumar, Dhruthi, G.K. Pramod, P. Samrat, M. Sadashiva, A Critical Review on Heat Treatment of Aluminium Alloys, Mater. Today Proc. **58** 71–79 (2022) https://doi.org/10.1016/j.matpr.2021.12.586
55. ASTM E8, ASTM E8/E8M standard test methods for tension testing of metallic materials 1, Annu. B. ASTM Stand. **4,** 1–27(2010) https://doi.org/10.1520/E0008
56. V. 238–100, Test specification: plate bending test for metallic materials, 2017. https://webshop.vda.de/VDA/en/vda-238-100-in-bearbeitungin-progress.
57. M. Negozio, A. Segatori, R. Pelaccia, B. Reggiani, L. Donati, Experimental investigation and numerical prediction of the peripheral coarse grain (PCG) evolution during the extrusion of different AA6082 aluminum alloy profiles. Mater Charact **209**, 113723 (2024). https://doi.org/10.1016/j.matchar.2024.113723
58. H. Zhao, L. Sun, G. Zhao, J. Yu, F. Liu, X. Sun, Z. Lv, S. Cao, Abnormal grain growth behavior and mechanism of 6005A aluminum alloy extrusion profile. J. Mater. Sci. Technol. **157**, 42–59 (2023). https://doi.org/10.1016/j.jmst.2023.02.013
59. S.B. Kim, T.H. Park, H.G. Kim, S.M. Lee, H.K. Kim, The thickness of recrystallization layer and mechanical properties according to extrusion exit temperature. Trans. Mater. Process. **30**, 219–225 (2021)
60. J.A. Taylor, Iron-containing intermetallic phases in Al-Si based casting alloys. Procedia Mater. Sci. **1**, 19–33 (2012). https://doi.org/10.1016/j.mspro.2012.06.004
61. J.A. Österreicher, M. Kumar, A. Schiffl, S. Schwarz, G.R. Bourret, Secondary precipitation during homogenization of Al-Mg-Si alloys: influence on high temperature flow stress. Mater. Sci. Eng. A **687**, 175–180 (2017). https://doi.org/10.1016/j.msea.2017.01.074
62. T. Minoda, H. Uchida, K. Shibue, H. Yoshida, Influence of iron content on mechanical properties of Al-Mg-Si alloy sheets. J. Japan Inst. Light Met. **53**, 523–527 (2003). https://doi.org/10.2464/jilm.53.523
63. J. a Taylor, The Effect of Iron in Al-Si Casting Alloys, 35th Aust. Foundry Inst. Natl. Conf. (2004) 148–157.
64. J. Hirsch, K. Lücke, Overview no. 76. Mechanism of deformation and development of rolling textures in polycrystalline f.c.c. metals-II. Simulation and interpretation of experiments on the basis of Taylor-type theories. Acta Metall. **36**, 2883–2904 (1988). https://doi.org/10.1016/0001-6160(88)90173-3
65. Y. Liu, M. Liu, X. Chen, Y. Cao, H.J. Roven, M. Murashkin, R.Z. Valiev, H. Zhou, Effect of Mg on microstructure and mechanical properties of Al-Mg alloys produced by high pressure torsion. Scr. Mater. **159**, 137–141 (2019). https://doi.org/10.1016/j.scriptamat.2018.09.033
66. Y. Wang, T. Yang, Q. Lu, K. Li, Z. Wang, Y. Du, Grain size refinement and enhanced precipitation strengthening in a hot extruded 6xxx Al alloy without homogenization. Mater. Characteriz. **198**, 112718 (2023). https://doi.org/10.1016/j.matchar.2023.112718
67. E. Nes, N. Ryum, O. Hunderi, On the Zener. Acta Mater. **33**, 11–22 (1985)
68. Y. Wang, B. Yang, M. Gao, E. Zhao, R. Guan, Microstructure evolution, mechanical property response and strengthening mechanism induced by compositional effects in Al–6 Mg alloys. Mater. Des. **220**, 110849 (2022). https://doi.org/10.1016/j.matdes.2022.110849
69. S. Naghdy, L. Kestens, S. Hertelé, P. Verleysen, Evolution of microstructure and texture in commercial pure aluminum subjected to high pressure torsion processing. Mater Charact **120**, 285–294 (2016). https://doi.org/10.1016/j.matchar.2016.09.012
70. F. Montheillet, M. Cohen, J.J. Jonas, Axial stresses and texture development during the torsion testing of Al, Cu and α-Fe. Acta Metall. **32**, 2077–2089 (1984). https://doi.org/10.1016/0001-6160(84)90187-1
71. J. Chen, W.J. Poole, N.C. Parson, The effect of through thickness texture variation on the anisotropic mechanical response of an extruded Al-Mn-Fe-Si alloy. Mater. Sci. Eng. A **730**, 24–35 (2018). https://doi.org/10.1016/j.msea.2018.05.105
72. S. Suwas, S. Mondal, Texture evolution in severe plastic deformation processes. Mater. Trans. **60**, 1457–1471 (2019). https://doi.org/10.2320/matertrans.MF201933
73. Y. Mahmoodkhani, M.A. Wells, N.C. Parson, J. Chen, W.J. Poole, R.T. Aluminium, Influence of Extrusion Die Bearing Geometry on Surface Grain Structure and Texture, (n.d.) 767–780.
74. Y. Mahmoodkhani, J. Chen, M.A. Wells, W.J. Poole, N.C. Parson, The effect of die bearing geometry on surface recrystallization during extrusion of an Al–Mg–Si–Mn alloy. Metall. Mater. Trans. A **50**, 5324–5335 (2019). https://doi.org/10.1007/s11661-019-05437-0
75. W.H. Van Geertruyden, H.M. Browne, W.Z. Misiolek, P.T. Wang, Evolution of surface recrystallization during indirect extrusion of 6xxx aluminum alloys. Metall. Mater. Trans. A Phys. Metall. Mater. Sci. **36**, 1049–1056 (2005). https://doi.org/10.1007/s11661-005-0298-6
76. R. Fu, Y. Huang, Y. Liu, H. Li, Microstructural evolution and dynamic recrystallization behavior of the homogenized 2195 Al–Li alloy during hot deformation. Met. Mater. Int. **29**, 2605–2622 (2023). https://doi.org/10.1007/s12540-023-01397-8
77. L. De Pari, W.Z. Misiolek, Theoretical predictions and experimental verification of surface grain structure evolution for AA6061 during hot rolling. Acta Mater. **56**, 6174–6185 (2008). https://doi.org/10.1016/j.actamat.2008.08.050
78. H.J. McQueen, Development of dynamic recrystallization theory. Mater. Sci. Eng. A **387**, 203–208 (2004). https://doi.org/10.1016/j.msea.2004.01.064
79. H.J. McQueen, O. Knustad, N. Ryum, J.K. Solberg, Microstructural evolution in Al deformed to strains of 60 at 400 °C. Scr. Metall. **19**, 73–78 (1985). https://doi.org/10.1016/0036-9748(85)90268-6
80. D. Song, Y. Jia, Q. Li, Y. Zhao, W. Zhang, Effect of initial Fe content on microstructure and mechanical properties of recycled

Al–7.0Si–Fe–Mn alloys with constant Mn/Fe ratio. Materials (2022). https://doi.org/10.3390/ma15041618

81. J. Mathew, G. Remy, M.A. Williams, F. Tang, P. Srirangam, Effect of Fe intermetallics on microstructure and properties of Al–7Si alloys. Jom **71**, 4362–4369 (2019). https://doi.org/10.1007/s11837-019-03444-5
82. A. Elasheri, N. Parson, X.G. Chen, Microstructure, tensile and bending properties of extruded Al–Mg–Si 6xxx alloys with individual and combined additions of Zr and Mn. Mater. Sci. Eng. A **894**, 146156 (2024). https://doi.org/10.1016/j.msea.2024.146156
83. E. Nes, N. Ryum, O. Hunderi, On the zener drag. Acta Metall. **33**, 11–22 (1985). https://doi.org/10.1016/0001-6160(85)90214-7
84. F. Liu, S. Chen, Q. Dong, J. Qin, Z. Li, B. Zhang, H. Nagaumi, Tailoring microstructure and mechanical properties of Al-Mg-Si-Cu alloy with varying Mn and/or Cr additions. Mater. Sci. Eng. A **892**, 146053 (2024). https://doi.org/10.1016/j.msea.2023.146053
85. V. Espeseth, D. Morin, C. Tekoğlu, T. Børvik, O.S. Hopperstad, Ductile tearing of aluminium plates: experiments and modelling. Int. J. Fract. **242**, 39–70 (2023). https://doi.org/10.1007/s10704-023-00701-2
86. F. Šebek, P. Salvet, P. Boháč, R. Adámek, S. Věchet, T. Návrat, J. Zapletal, M. Ganjiani, Size effect on the ductile fracture of the aluminium alloy 2024–T351. Exp. Mech. **64**, 1483–1495 (2024). https://doi.org/10.1007/s11340-024-01108-3
87. H. Takeda, A. Hibino, K. Takata, Influence of crystal orientations on the bendability of an Al–Mg–Si alloy. J. Jpn. Inst. Light Met. **60**, 231–236 (2010). https://doi.org/10.2464/jilm.60.231
88. G.M. Ludtka, D.E. Laughlin, The influence of microstructure and strength on the fracture mode and toughness of 7XXX series aluminum alloys. Metall. Trans. A **13**, 411–425 (1982). https://doi.org/10.1007/BF02643350